Journal of Molecular Liquids 413 (2024) 126047

Contents lists available at ScienceDirect

Journal of Molecular Liquids

journal homepage: www.elsevier.com/locate/molliq

Ramification and labyrinth instabilities in a ferroelectric nematic fluid exposed to electric fields

Marcell Tibor Máthé [a,b], Hiroya Nishikawa [c], Fumito Araoka [c,*], Antal Jákli [a,d,e,*], Péter Salamon [a,*]

[a] Institute for Solid State Physics and Optics, HUN-REN Wigner Research Centre for Physics, P.O. Box 49, Budapest H-1525, Hungary
[b] Eötvös Loránd University, P.O. Box 32, H-1518 Budapest, Hungary
[c] RIKEN Center for Emergent Matter Science, 2-1 Hirosawa, Wako, Saitama, 351-0198, Japan
[d] Materials Sciences Graduate Program and Advanced Materials and Liquid Crystal Institute, Kent State University, Kent, OH 44242, USA
[e] Department of Physics, Kent State University, Kent, OH 44242, USA

ARTICLE INFO

Keywords:
Ferroelectric nematic liquid crystal
Electric field induced interfacial instability
Ramification instability
Labyrinth instability
Liquid bridge
Droplet

ABSTRACT

Recently, an electric field induced interfacial instability of ferroelectric nematic liquid crystals was reported (Sci. Rep. 13:6981 (2023)). It was found that above a threshold, the interface of the fluid with air undergoes a fingering instability or ramification. Here it is shown that by increasing the voltage between the two sides of a ferroelectric liquid bridge, the primary fractal-like ramification is followed by a secondary labyrinthine instability. The instabilities are well distinguishable by their completely different morphologies, and they both emerge sharply at distinct threshold voltages. The critical requirements for the instabilities are presented and the crucial role of the insulating layers on the electrodes is discussed. Experiments and finite element method simulations suggest that the main driving force of the ramification and labyrinthine instabilities is an unexpected electric field component parallel to the electrodes.

1. Introduction

Ferroelectric fluids exhibiting spontaneous electric polarization ($\mathbf{P_s}$) were first realized in 2017 [1,2] although theoretically they were predicted [3,4] much earlier. Strikingly, the polar nature in these ferroelectric nematic liquid crystals (FNLCs) has intrinsic origin: even single component organic fluids can be ferroelectric if the molecular dipole moments are sufficiently large and the molecules are elongated along the dipole moment [5,6]. The properties and the behaviour of FNLCs [7] in electric field are unique, and their extreme sensitivity to electric fields promise useful applications e.g., in displays [8] or as electro-mechanical transducers [9,10].

Similar to conventional nematic liquid crystals [11], FNLCs are composed of elongated molecules with long range orientational order. At a given position $\boldsymbol{r}$, the average direction of the long molecular axes is described by the director $\boldsymbol{n}(\boldsymbol{r})$. The nematic head–tail symmetry $\boldsymbol{n} = -\boldsymbol{n}$ is broken in FNLCs, where the emerged spontaneous polarization $\boldsymbol{P_s}$ is parallel to $\boldsymbol{n}$. The magnitude of polarization is typically $|\boldsymbol{P_s}| \sim 5\ \mu C/cm^2$ [7,8,12], which is several times smaller than of typical ferroelectric crystals [13]. The measured relative permittivities of FNLCs were also found in the range of $\varepsilon \sim 10^4$ [1,14–22], promising their usage in supercapacitors variable by external stimuli [23].

Such large spontaneous polarization and permittivity combined with the much larger responsiveness to external fields than of solid ferroelectrics makes FNLCs unique. The presence of $\boldsymbol{P_s}$ facilitates the emergence of bound charges even without external electric field. At an interface, the surface charge density is given by $\rho_s = \boldsymbol{P_s}\cdot\boldsymbol{u}$, where $\boldsymbol{u}$ is the surface normal vector. In bulk, splay deformation generates bound charges with the density $\rho_b = -\nabla\boldsymbol{P_s}$. In general, electric fields generated by the charges increase the electrostatic energy, therefore the system tends to avoid a polarization splay and a polarization component along the surface normal. The presence of bound charges stabilizes long fluid threads of FNLCs [24,25] and leads to fluid superscreening [26].

On one hand, large dielectric permittivity suggests the possibility of a giant dielectrowetting effect in FNLCs at remarkably low voltages, since the threshold voltage scales with the square root of the fluid's permittivity [27–29]. This would mean an electric field induced homogeneous spreading of the fluid making large area thin films with apparently zero

* Corresponding authors.
E-mail addresses: fumito.araoka@riken.jp (F. Araoka), ajakli@kent.edu (A. Jákli), salamon.peter@wigner.hun-ren.hu (P. Salamon).

https://doi.org/10.1016/j.molliq.2024.126047
Received 10 June 2024; Received in revised form 28 August 2024; Accepted 14 September 2024
Available online 16 September 2024

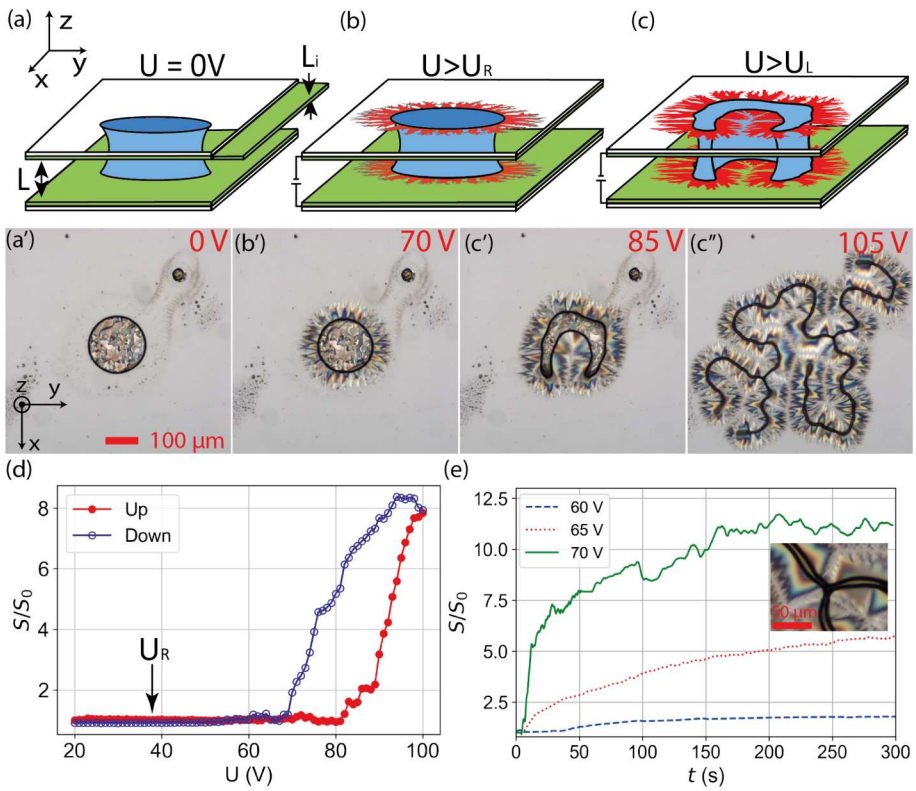

Fig. 1. Schematic illustration and micrographs of the ferroelectric nematic sample in the liquid bridge geometry without electric field (a-a') and above a threshold field, leading to ramification (b-b') and labyrinthine instability (c-c'-c"). U is the (rms) amplitude of AC voltage applied between the bounding plates, providing an electric field parallel to the z-direction far from the bridges. Snapshot (c') represents the state slighty above the threshold field of the labyrinthine instability, while (c") shows the morphology at higher voltage. The shape of the meniscus line of the liquid bridge (black circles in (a') and in (b') and black curves in (c') and in (c")) is affected only by the secondary, labyrinthine instability. (d) Relative length (S/S_0) of the meniscus line as a function of U with slowly increasing (up) and decreasing (down) voltages. $L = 12$ μm is the cell gap and $L_i = 1.5$ μm the insulation layer thickness. (e) Time dependence of the the relative length of the meniscus line after step-wise switching on the voltage from zero to different levels: (blue) 60 V, (red) 65 V, (green) 70 V. The cell parameters were: $L = 14$ μm and $L_i = 1.5$ μm.

contact angle. On the other hand, the analogy between ferromagnetic and ferroelectric phenomena implies that one could observe a spectacular spiky pattern on top of the free surface of FNLCs in electric field, similar to the Rosenweig-type normal field instability [30,31] in ferrofluids exposed to magnetic field.

Recently we reported that, instead of a uniform spreading or spiky undulation of the free surface, a fractal-like ramification instability occurs, which is localized to the contact line [32]. Above a threshold AC voltage applied on FNLC droplets, this phenomenon results in stationary branched fluid structures at the contact line of the FNLC with the substrate and the surrounding air. It was also found in various electrode geometries that the length of the branches can be adjusted by the amplitude and frequency of the applied voltage [32]. A similar instability was observed in FNLC droplets placed either on top [33,34], near [35] and in between [36,37] ferroelectric lithium-niobate (LN) crystals. Since the electric field around an LN crystal cannot be adjusted in fine steps, a dynamic jetting of the branches was seen. However, by optical fields, either the control of the jets [38,39] and the positioning of the droplets [40] was achieved. This phenomenon was explained by an effect analogous to the Rayleigh instability of charged fluid droplets [33].

Here we show that there are two distinct AC electric field induced interfacial instabilities in liquid bridges of ferroelectric nematic fluids sandwiched between planar electrodes. The primary instability is the ramification process of the contact line localized in the vicinity of the bounding plates, while the secondary instability affecting the entire meniscus is analogous to a Rosensweig-type labyrinthine instability observed in magnetic ferrofluids [31,41]. Via theoretical calculations and finite element method simulations we will explain the physical mechanism and the prerequisites of the instabilities and will show the crucial role of the thin insulating layers on the electrodes.

2. Experimental results

Our experiments were performed in a liquid bridge geometry sketched in Fig. 1a using FNLC RM734 (see details in the Methods section). To prepare a liquid bridge, a sessile droplet of a ferroelectric nematic compound was squeezed between two parallel flat substrates covered by transparent conductive indium-tin-oxide (ITO) layers. To block direct charge transfer and electrochemical reactions with the liquid crystal, the inner surfaces of the electrodes were coated by 50–5000 nm thick insulating crosslinked SU8 polymer films (marked as green layers in Fig. 1a-c). As we will see later, the blocking layers on the electrodes not only prevent the degradation of the liquid crystal under electric fields, but also play a key role in the emergence of the distinct interfacial instabilities of the fluid bridges.

The behaviour of FNLC bridges was investigated by applying AC voltages across the electrodes, so that the resulting oscillating electric field was normal to the substrates (parallel to z-direction) far from the bridges. Unless it is indicated differently, all measurements were carried out in the ferroelectric nematic phase ~5 °C below the nematic - ferroelectric nematic transition temperature.

In the initial state, the liquid crystal is in contact with both surrounding flat plates and forms a liquid bridge as shown in Fig. 1a. The radius of the droplets and the cell gap were in the micrometre range, thus gravitational effects to the shape of the liquid bridge can be neglected. Under these conditions, the meniscus line appearing at the curved liquid–air interface can be approximated by one of the Delaunay's surfaces: elliptic, hyperbolic, or catenoid [42]. As the contact

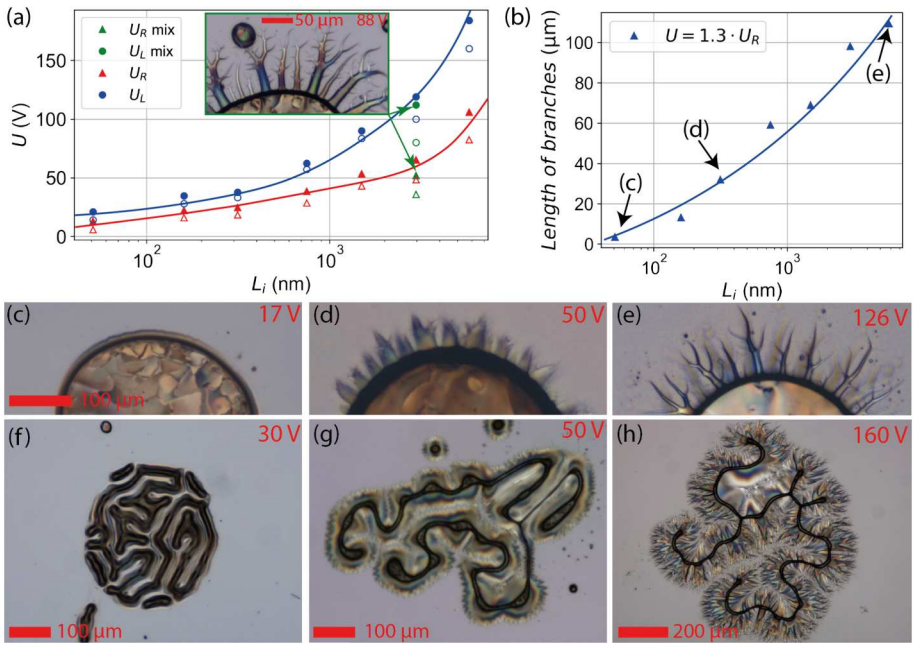

Fig. 2. Summary of the effect of the insulating layers' thickness (L_i) on the ramification and labyrinthine instabilities. (a) Dependence of the threshold voltages of the ramification (U_R) and the labyrinth instability (U_L) on L_i. Filled (empty) markers correspond to increasing (decreasing) voltages. The green data points show a 'mixed' cell with different layer thicknesses on the top and bottom substrates: $L_i^{bottom} = 260$ nm and $L_i^{top} = 5788$ nm, with the corresponding image in the inset. The abscissa was calculeted as $L_i = (L_i^{bottom} + L_i^{top})/2$. In the mixed cell, the long branches emerge on the side with the thicker blocking layer. (b) Length of the longest branch as a function of L_i recorded at $U = 1.3 \cdot U_R$. The gap sizes of the cells were in the range 12 µm-20 µm. Snapshot of the ramification instability in cells with different blocking layer thickness: (c) 51 nm, (d) 750 nm and (e) 5788 nm at $f = 1$ kHz. The appearance of droplets at $U = 1.3 \cdot U_L$ above the threshold of the labyrinth instability driven at $f = 1$ kHz with (f) 51 nm, (g) 315 nm and (h) 2966 nm blocking layer thicknesses.

angle of RM734 on SU8 is smaller than 90° (~30°-50°), the FNLC-air interface is curved, and the meniscus is concave with a diabolo shape. At zero electric field, the microscope images reveal a black circular contour line (see Fig. 1a') due to the refraction of light on the curved meniscus, and we refer to it as meniscus line. We note that the meniscus line and contact line (line on the solid substrate where the gas phase meets the fluid) are different.

As seen in Fig. 1b, above a threshold voltage U_R the ramification instability described in [32] occurs, which takes place at the contact line, while the meniscus line is unchanged. Further increasing the voltage, a continuous growth of branches takes place up to a well-defined second critical voltage U_L where another instability emerges. During this secondary instability the entire meniscus line loses its initially circular shape by involving complicated concave closed loop, such as shown in Fig. 1c'. At even higher voltages (Fig. 1c"), the closed meniscus line forms complex and branched structures resembling to labyrinths, therefore we call this labyrinthine instability.

To characterize this secondary labyrinthine instability, we plotted the length of the meniscus line S relative to the S_0 initial circumference as a function of U in Fig. 1d in increasing and decreasing voltage at $f = 1$ kHz. The length of the meniscus line starts to grow sharply just above the threshold voltage U_L, and it grows continuously as we increased the applied field up to a point, when the meniscus-lines break to parts. If we start to decrease the field before it breaks up, the initial circular shape reforms, therefore the phenomenon exhibits reversible behaviour. A wide hysteresis (~ 20 V) is seen in Fig. 1d between the $S/S_o(U)$ in increasing (red) and decreasing (blue) voltages. This may be due to a very slow dynamics of the system or a strong first order nature of the labyrinthine instability. We note that the waiting time between two subsequent data points was 10 s.

On another sample, we investigated the behaviour of the relative meniscus line length as a function of time, after stepwise switching on the voltage to three different levels from 0 V at $t = 0$ s (Fig. 1e). The experiments show that well over 100 s is required to reach the final state. Stepping up to a voltage close to the threshold ($U = 60$ V) the shape-change of the drop took over 40 s. Interestingly, three-way junctions appear in well-developed meniscus lines undergone the labyrinth instability as seen in the inset of Fig. 1e. Such junctions in the labyrinthine structure typically appear at voltages significantly higher than U_L. Note that in three-way junctions, the parts of the meniscus line close an angle at about ~120° with each other, which regular shape is the consequence of the energy minimization accounting for the radii of curvature and the electrostatic repulsion between the branches [32].

We performed measurements with cells without blocking layers, so that the FNLC was in direct contact with the conducting ITO layers. In this case, neither the ramification nor the labyrinth instability could be observed. This shows that the thickness of the insulating (or blocking) layer on the electrodes has a key role in the formation of both instabilities. To reveal how the insulating layer affects the emergence of the ramification and labyrinthine instabilities, we performed studies as a function of SU8 layer thickness in the range from 51 nm to 5788 nm.

Fig. 2a shows $U_R(L_i)$ and $U_L(L_i)$ in cells with approximately 15 μm gap size. Both U_R and U_L increase with the thickness of the insulating layers, due to the voltage attenuation between the FNLC and the SU8 layer. Fig. 2b shows that the length of the branches of the ramification instability strongly depends on the blocking layer thickness. For the thinnest (~51 nm) blocking layer the branches are about ~ 3 µm long as seen in Fig. 2c, while this length is more than 100 µm, when $L_i \sim$ μm (Fig. 2e). Cells with the same L_i on both sides ($L_i = L_i^{top} = L_i^{bottom}$), the branches have similar lengths on each side. We also prepared a 'mixed' cell with $L_i^{top} = 5788$ nm and $L_i^{bottom} = 260$ nm. In this case, the long branches can be observed only on the thicker blocking layer, as presented in the inset of Fig. 2a. Note that U_R of the mixed cell is close to that of the cell with uniform $L_i = (L_i^{top} + L_i^{bottom})/2$.

As $U_R < U_L$, it is impossible to characterize the labyrinth instability by itself. However, we found that the morphology of this instability is not as sensitive to the blocking layer thickness as of the ramification.

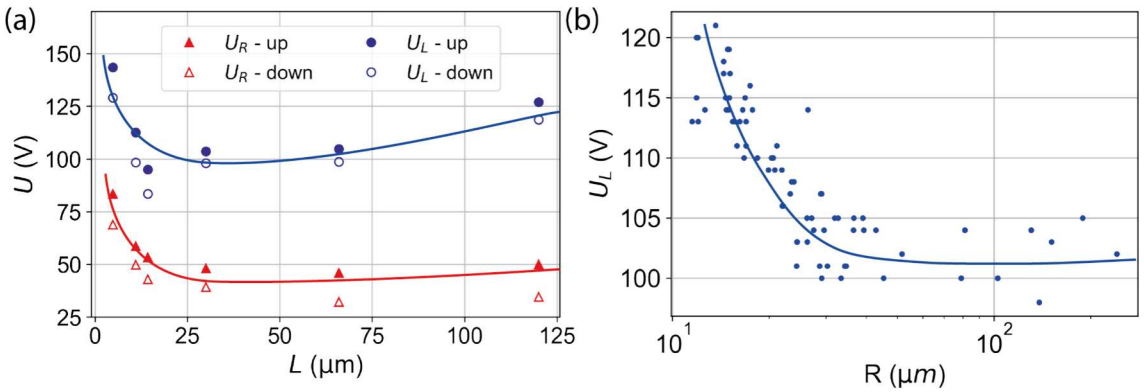

Fig. 3. Summary of the effect of the gap size L and bridge radius R on U_R and U_L. (a) $U_L(L)$ and $U_R(L)$ for $L_i = 1.5$ μm. (b) $U_L(R)$ at $f = 1$ kHz with 1.5 μm blocking layers and 12.4 μm gap.

Fig. 2(f–h) show liquid bridges at $U = 1.3 \cdot U_L$ and $f = 1$ kHz with increasing values of L_i. We can see that the closed loops of the meniscus lines (dark curves) are separated due to the repulsion between the branches generated by the ramification. An increasing L_i results in longer branches even at voltages higher than U_L, following the tendency observed in Fig. 2b with no labyrinthine instability (and therefore no possible interaction of branches growing towards each other). Consequently, the structures of the labyrinths at higher L_i become sparser. The behaviour of the instabilities can be seen in Supplementary Video S1, S2, and S3 with $L_i =$ 260 nm, $L_i =$ 1500 nm, and $L_i =$ 2966 nm, respectively.

We also investigated the behaviour of the interfacial instabilities in cells with different gap sizes L. In this measurement, the diameter of the liquid bridges was kept approximately the same and the thickness of the blocking layer was $L_i = 1.5$ μm. For both instabilities, we found that the threshold voltages are the highest at low L. By increasing the cell thickness up to about $L \approx 15$ μm, both thresholds (U_R and U_L) drop sharply (see Fig. 3a), then in the range of 15 μm $< L <$ 75 μm, U_R and U_L are approximately constant. At the higher end of the studied gap range, we can observe a slight increase in U_L, while there is no

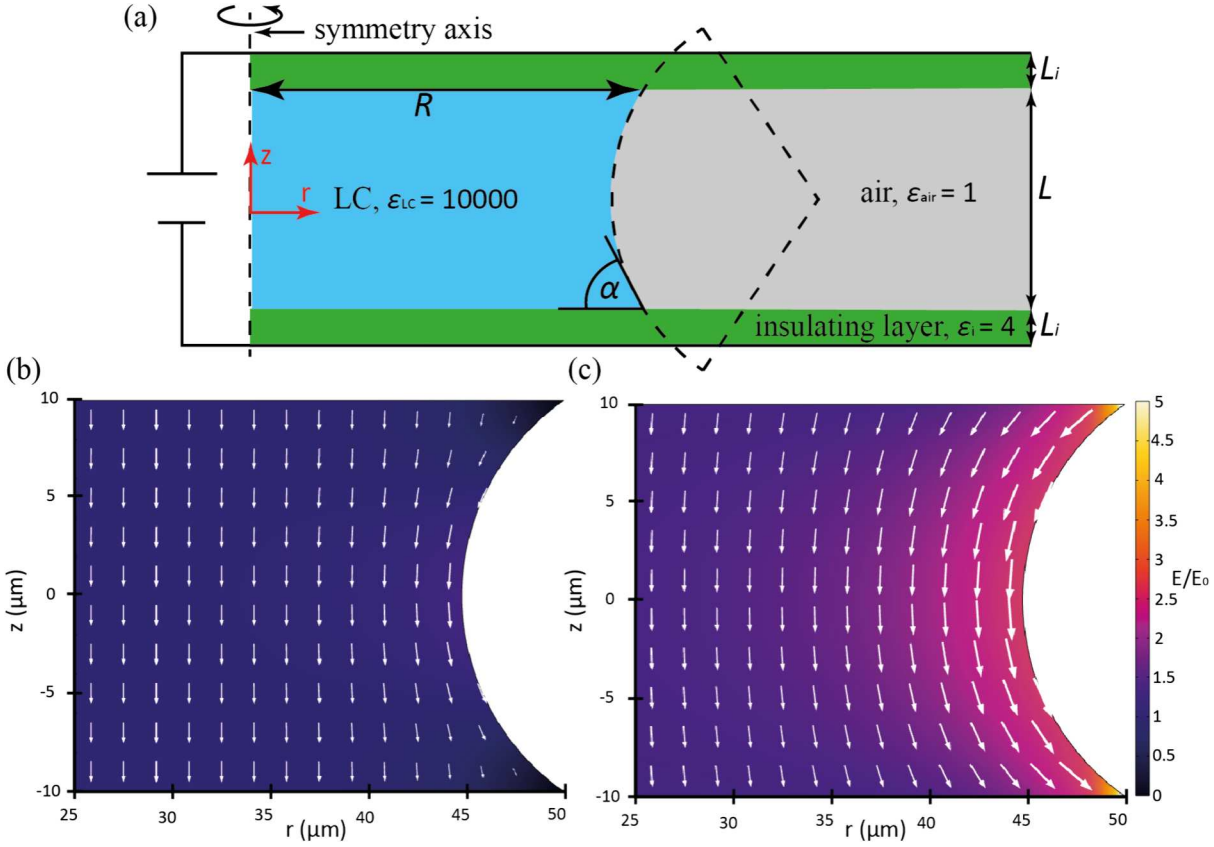

Fig. 4. Illustration of the physical parameters and the simulated field distribution. (a) The schematics and the parameters of the simulated geometry with circular meniscus line profile. The parameters: L_i: insulating layer thickness, L: cell gap, R: base radius of the liquid bridge, α : contact angle and ε_{LC}, ε_i, ε_{air} are the relative permittivity of liquid crystal, insulating layer and air. Distribution and magnitude of the electric field in the liquid bridge calculated by COMSOL Multiphysics: (b) $L_i = 0$ and (c) $L_i = 1.5$ μm. The arrows and the colour-map represents the normalised electric field E/E_0, where $E_0 = U\left(2L_i\frac{\varepsilon_{LC}}{\varepsilon_i} + L\right)^{-1}$ is the electric field inside the liquid crystal far from the meniscus. The gap was $L = 20$ μm with $\alpha = 35°$.

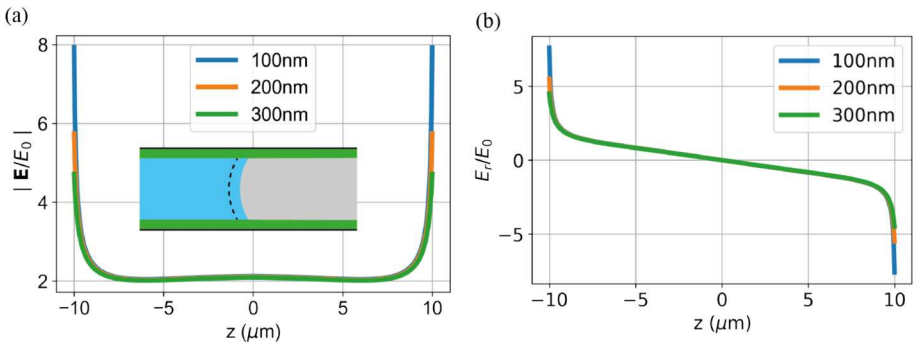

Fig. 5. Simulated normalized electric field dependence inside the liquid crystal. (a) Absolute value of the normalised electric field ($|\boldsymbol{E}/E_0|$) and (b) the normalised radial component of the electric field E_r/E_0 in the liquid bridge along the curved meniscus (indicated by dashed line in the inset) at 100 nm, 200 nm, and 300 nm distance from the air interface plotted versus the z-coordinate. ($L_i = 1.5$ μm, $L = 20$ μm, and $\alpha = 35°$).

significant change in $U_R(L > 75\ \mu\text{m})$. The dynamics of the instabilities can be seen on the Supplementary Video S4 and S5 with $L = 4.8$ μm, and $L = 66$ μm, respectively.

Even for well-developed labyrinths well above U_L, the original one piece of the liquid bridge can be restored by slowly decreasing the voltage, although the position may change (see Supplementary Video S6). After rapid turn-off of the voltage may result in multiple bridges with smaller diameters. Furthermore, at high voltages the meniscus lines can break up causing the fragmentation of the liquid bridge. Turning off the voltage after such a case also creates a distribution of smaller liquid bridges with circular bases. Once the bridges break up to smaller pieces, they cannot merge again later due to the repulsion between the tips of the branches generated by the ramification.

In Fig. 3b, we can see how U_L depends on the initial radius of the liquid bridges with $f = 1$ kHz driving voltage, $L_i = 1.5$ μm, and $L = 12.4$ μm. It can be seen that $U_L(R)$ decreases toward higher R. We note that U_R is basically independent of R.

In this paper, we only discuss the primary ramification and secondary labyrinthine instabilities. We note that at even higher voltages an actively moving state of the liquid bridges emerge, which phenomenon was published recently [43].

3. Discussion

3.1. Simulation of the electric field

Our experiments showed that the presence of insulating layers on the electrodes plays a crucial role on the formation of the studied interfacial instabilities of ferroelectric nematic fluid bridges. To understand this, we simulated the electric field distribution in the liquid bridge geometry using the finite element method with COMSOL Multiphysics by solving the Poisson equation.

The schematic of the studied geometry can be seen in Fig. 4a. In our simulations, we approximated the shape of the meniscus with a circular profile [42]. The parameters of the simulated liquid bridge are the base radius R, the cell gap L and contact angle α. The liquid bridge is sandwiched between two planar insulator sheets of thickness L_i. Outside the liquid crystal between the insulating layers the third medium is supposed to be air. Due to the cylindrical symmetry (r, φ, z) coordinates are used. The symmetry axis is along z, and $(r, \varphi, z = 0)$ is a mirror plane in the studied geometry. We prescribe constant electric potentials $\phi\left(z = +\frac{L}{2} + L_i\right) = -\frac{U}{2}$, and $\phi\left(z = -\frac{L}{2} - L_i\right) = +\frac{U}{2}$ on the top and bottom electrodes. The base radius of the insulating layer is R_i, which was chosen to be sufficiently high so that the results near the contact line and the meniscus were unaffected by the choice.

For simplicity, we consider an isotropic model, where the dielectric anisotropy and the spontaneous polarization are neglected. The relative permittivity of the FNLC, the insulating layer, and the air was denoted by ε_{LC}, ε_i, and ε_{air}, respectively. The polar nature of the studied ferroelectric nematic material is taken into account only by considering a huge effective relative permittivity: $\varepsilon_{LC} = 10000$. Although such high apparent permittivities were indeed reported [1,14–22,44], they are likely artifact, and what measured is the capacitance of the insulating layers [45,46]. We note however, that our results to be presented are qualitatively the same even at lower ε_{LC}; the only requirement is that the three permittivities (ε_{LC}, ε_i, and ε_{air}) need to be different.

The radius of the droplet was set to $R = 50$ μm, and the radius of the electrode (and insulating layer) was $R_i = 100$ μm, while the maximum mesh size inside the liquid crystal was 100 nm. We emphasize that our simple model does not aim to give a perfect description of the studied phenomena, our goal is to qualitatively shed light on important aspects. Developing a more realistic model including anisotropy, spontaneous polarization of the liquid crystal and AC voltage driving including ionic conductivity is beyond the scope of the present work and may be a subject of further studies.

Analytically, we can calculate the electric field in the dielectric liquid crystal between two insulating layers in that case, when the liquid crystal entirely fills the cell. The solution has only z-component with the magnitude $E_0 = U\left(2L_i\frac{\varepsilon_{LC}}{\varepsilon_i} + L\right)^{-1}$. This result shows a strong reduction of the electric field in presence of insulating layers. In our geometry, the electric field is expected to approach E_0 far from the edges.

Having an additional, vertical boundary within the cell between the liquid crystal and air leads to qualitatively different electric field distribution close to this boundary, but only when insulating layers are present. The electric field $\mathbf{E} = (\mathrm{E_r}, \mathrm{E}_\varphi, \mathrm{E_z})$ inside the liquid crystal is shown in Fig. 4b and Fig. 4c without and with insulating layers between the FNLC and the electrodes, respectively. The normalised electric field ($\boldsymbol{E}/E_0$) is represented by white arrows and the value of $|\boldsymbol{E}/E_0|$ is displayed on the colour map. When we set $L_i = 0$ (Fig. 4b), the FNLC is in direct contact with the electrodes, thus the electric field must be along the z axis at the top and bottom boundaries. In the central part of the FNLC, the field has only vertical component, but close to the FNLC-air interface, due to the curvature of the meniscus, $\boldsymbol{E}$ has also a small radial component. Away from the meniscus $|\boldsymbol{E}/E_0| \approx 1$, but closer to the triple (FNLC-air-ITO) junction, the magnitude of the field decreases. In contrast, as Fig. 4c shows, when the electrodes were covered by 1.5 μm thick insulating layers, the structure of the electric field entirely changed. Near the meniscus, the magnitude of the field significantly increased, and a strong radial electric field component emerged close to the triple (FNLC-air-SU8) junction. In bulk, $\boldsymbol{E}$ has only vertical component and the value of $|\boldsymbol{E}/E_0|$ decreases to ≈ 1.

Fig. 5a and Fig. 5b show the absolute value and the radial component of the electric field as a function of the z along a line (marked by black dashed line in the inset of Fig. 5a) at 100 nm, 200 nm and 300 nm

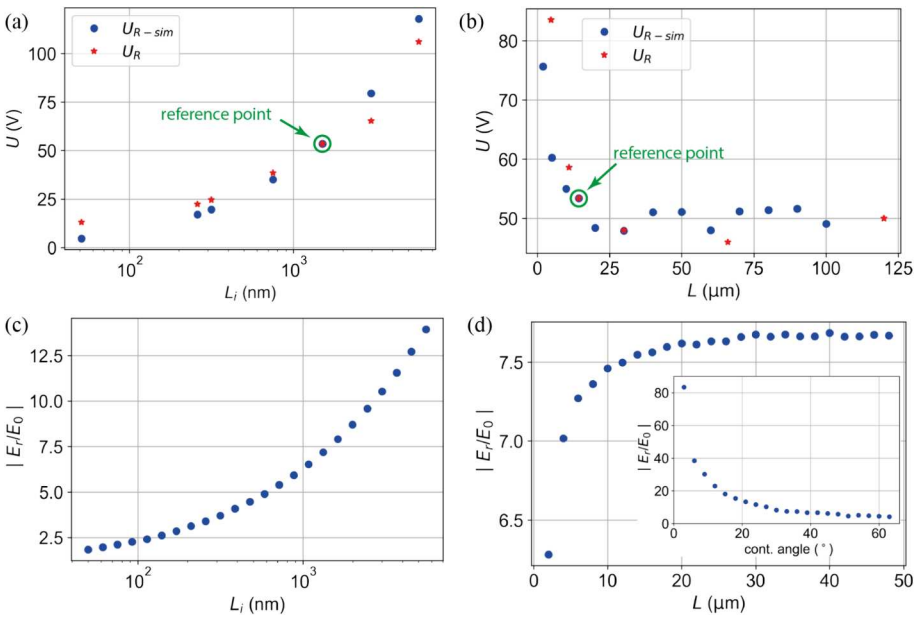

Fig. 6. Comparison of the threshold voltages of ramification from the experiments U_R (red) and derived from the simulations U_{R-sim} (blue). (a) As a function of the insulating layer thickness (L_i) and (b) as a function of the gap size (L). The reference radial electric field value obtained in the simulation was calculated from the measurement with $L_i = 1.5$ μm and $L = 15$ μm at $U_R = 53.4$ V. At this point the simulated and measured values coincide. The normalised radial electric field obtained from the simulations as a function of the insulating layer thickness (c) ($L = 20$ μm, U=20 V) and gap size (d) ($L_i = 1.5$ μm, U=20 V). Inset to (d) ($L = 20$ μm, $L_i = 1.5$ μm, U=20 V) shows the contact angle dependence of the normalised radial electric field obtained from the simulations.

distance from the meniscus. Both the absolute value and the radial component are larger close to the boundary. This agrees with our experimental observation that the ramification emerges at the contact line [32]. Near the triple junction of materials, the electric field becomes more than double of the bulk value, showing significant edge effect. The appearance of the radial electric field component is also spectacular (see Fig. 5b); the direction of E_r is the opposite on the top and bottom sides and depends on the polarity of the applied voltage.

To compare the simulated and measured data, we computed the radial component of the electric field (E_{r-ref}) at the junction of the three media for the cell with $L_i = 1.5$ μm and $L = 15$ μm at a voltage of 53.4 V. This voltage is consistent with the threshold voltage of the ramification instability in a cell with the same parameters. The E_{r-ref} field was then taken as the reference value for the threshold electric field. In the simulation, the gap size and insulating layer thickness of the cell were systematically varied. Subsequently, the voltage (denoted by U_{R-sim}) was adjusted to achieve the reference E_{r-ref} electric field value.

Fig. 6(a and b) illustrate the dependence of U_{R-sim} on the layer thickness and gap size as determined from the E_{r-ref} reference field, respectively. The simulated data U_{R-sim} marked by blue colour, exhibit similar dependence as the measured data U_R marked by red colour. The coincidence of the measured and simulated data indicates that the origin of the ramification instability is indeed from the presence of radial electric field because of the insulating layer.

Fig. 6c shows the layer thickness dependence of the normalised radial electric field ($|E_r/E_0|$). The value of $|E_r/E_0|$ increases significantly for thicker blocking layers, which is consistent with our observation that the tips are much longer for thicker insulating layers (see Fig. 2). The gap dependence of $|E_r/E_0|$ is illustrated in Fig. 6d, where the value of $|E_r/E_0|$ decreases significantly for $L < 15$ μm, which explains the increase of U_R for cells with small gap size (see Fig. 3a).

The simulated data in the inset of Fig. 6d show that the $|E_r/E_0|$ grew significantly when we decreased the contact angle at the triple junction. This dependence can further drive the instability as the emergence of the branches significantly decrease the contact angle [32].

3.2. Ramification instability

The ramification instability emerges at the contact lines, located on the bounding plates at the FNLC-air interface [32]. In general, the stability of the fluid interface is determined by the balance between the stabilizing surface tension and the destabilizing electrostatic forces. In our present case, in the liquid bridge geometry, a radial electric force at the contact line can be expressed as $F_e = E_r \cdot q$, where q represents an electric charge. The charge originates from the radial component of the polarization at the interface. Although in absence of external electric field the polarisation has only tangential component to minimize the electric free energy as observed in independent experiments [47–51], in presence of a radial electric field a torque acts on the polarisation, which tends to realign the polarisation field. Therefore, $\boldsymbol{P}$ will have a radial component at the FNLC-air interface, leading to a surface charge per unit area $\rho_s = \boldsymbol{P} \cdot \boldsymbol{u}$, where $\boldsymbol{u}$ is the surface normal vector. According to Fig. 5b, E_r , and therefore also ρ_s, has different signs at the top and the bottom of the liquid bridge, but the electrostatic driving force per unit area $p_e = E_r \cdot \rho_s$, has the same sign at both surfaces. At the threshold voltage this is balanced by the capillary pressure $p_c = \frac{2\gamma cos\alpha}{r_c}$, where γ denotes the surface tension and r_c is the radius of the protruding tip of an emerging branch. At the threshold, $p_e = p_c$, which we can use to estimate the surface charge density. With $\gamma = 10^{-2}$ $\frac{N}{m}$ [24], $E_r = 3.7 \cdot 10^5$ $\frac{V}{m}$ and $\alpha = 35°$, the surface charge density is estimated as $\rho_s \approx \frac{2\gamma cos(\alpha)}{E_r r_c} = 4.4 \cdot 10^{-2}$ $\frac{C}{m^2}$. This value is well approximated by the absolute value of the spontaneous polarization $\rho_s \approx 4.4$ $\frac{\mu C}{cm^2} \sim |\mathbf{P_s}|$ [8], which agrees with the observation that the spontaneous polarization is aligned along the branches.

Due to their finite conductivity, FNLC samples contain free charges. To test the effect of the ions, we doped a sample with a relatively high amount of tetrabutyl ammonium benzoate (TBABE) organic salt in the weight concentration of 1 % in RM734. We found no significant change in the threshold voltage of the ramification instability, showing that their influence in kHz range AC electric fields can be neglected.

We note that it was reported recently by Marni et al. [36] that fringing fields (including in-plane components) also play crucial role in

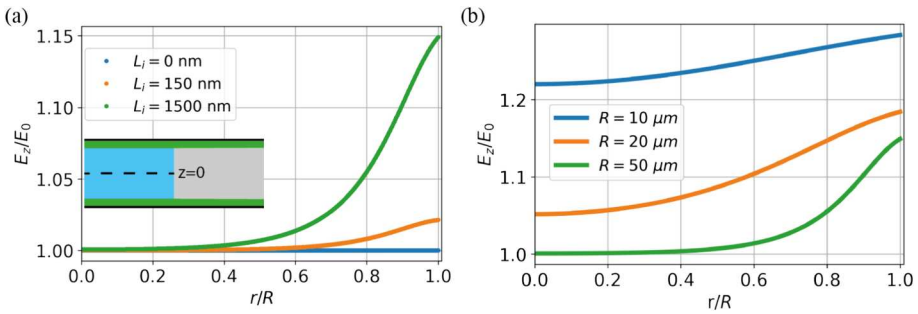

Fig. 7. The z component of the normalised electric field (E_z/E_0) as a function of the normalised radius (r/R) for different insulating layer thicknesses (a) and for different base radius values at $L_i = 1.5$ μm (b), where R is the base radius of the liquid bridge. E_z/E_0 was calculated in the middle of the liquid bridge at $z = 0$, marked by black dashed line in the left inset.

the formation of fluid jets from FNLC droplets confined between ferroelectric lithium niobate crystal slabs. In that case, the shape of electric field depends on how the spontaneous polarization direction is oriented in the bounding plates.

3.3. Labyrinthine instability

Instabilities like the secondary labyrinthine instability that we presented, have been observed in ferrofluids [41,52–59] and in dielectrics [41,60] in presence of magnetic and electric fields, respectively. In both cases, the materials were investigated in between two flat bounding substrates with large lateral sizes compared to their distance (in Hele-Shaw cells). In those previous studies the ferrofluids were sandwiched between insulating plexiglass spacers, which is an important similarity to our investigated geometries, where we deposited insulating layers on the electrodes. According to the theoretical analysis discussed for dielectrics [60], the F_L driving force of the labyrinthine instability is proportional with the inhomogeneity of the electric field: $F_L \sim (\varepsilon_f - \varepsilon_m) E_z \frac{dE_z}{dx}$, where ε_f is the permittivity of the investigated fluid and ε_m is the permittivity of the surrounding medium. The inhomogeneity of the field is due to the different voltage attenuation between the dielectrics with different permittivities.

In our simulations, we systematically changed the thickness of the insulating layer and the base radius of the liquid bridge (R_0). Fig. 7 illustrates the normalised radius dependence of E_z/E_0 for several insulating layer thicknesses at $R_0 = 50$ μm (Fig. 7a) and for several R_0 values at $L_i = 1.5$ μm (Fig. 7b). The value of E_z was measured at $z = 0$ along the black dashed line depicted in the inset of Fig. 7a. For simplicity, we assumed that the contact angle is 90°. In Fig. 7a, without insulating layer the $E_z/E_0 = 1$ in the whole sample. If $L_i \neq 0$, the vertical component of the field is larger closer to the FNLC-air interface and decreases to 1 close to the middle of the liquid bridge at $r/R_0 = 0$. If $L_i = 0$, the inhomogeneity of E_z disappears, which is consistent with the measurements as we could not observe the labyrinthine instability without blocking layer.

Fig. 3b shows that the labyrinthine instability is strongly affected by the original size of the liquid bridge, which is either due to the increasing effect of surface tension or the inhomogeneity of E_z as the droplet size decreases [61] (Fig. 7b). In dielectric fluids the required threshold voltage to induce the labyrinthine instability is in the range of 1–10 kV [60], while in our case it is an order of magnitude smaller. This is understandable as both F_L and $\frac{dE_z}{dx}$ are proportional with ε_f, which is in our case is > 100 [14], while $\varepsilon_f \approx 1 - 10$ for the dielectric oils [60].

4. Summary

In addition to a primary ramification described before [32] here we described a secondary labyrinthine interfacial instability in ferroelectric liquid bridges exposed to electric fields normal to the flat bounding substrates. Both effects appear above a sharp voltage threshold, but their morphology and localization are different. The ramification emerges at the contact line (at the substrates) forming flat hairy perimeter of the liquid bridges' edge, while the middle part of the bridge remains intact. In contrast, the labyrinth instability induces dramatic shape-change of the entire droplet leading to an enormous increase of the fluid surface.

Our results show that the critical requirement for the instabilities is the insulating layer on the electrodes, which is necessary to give rise to an in-plane electric field component at the substates for the ramification and a significant electric field gradient for the labyrinthine instability in the middle of the cell. The numerical simulations of the electric field distribution as a function of the insulating layer thickness, cell gap, and droplet size support our experimental findings. Our results are in accordance with previous studies on labyrinthine instabilities observed in ferrofluids [41,52–59] and in dielectrics [41,60] in presence of magnetic and electric fields, respectively, where spacer gaps at the field sources were required to observe the instabilities.

Such electrically tuneable fluid surface may give rise to applications in gas sensing or filtering, where a tuneable/switchable adsorbing surface is crucial. Another application idea is the use in microfluidic chemistry, where the reaction speed could be adjusted by on-demand modification of the adsorbing or catalysing surface. Furthermore, when the fluid undergoes the labyrinthine instability, air channels penetrate from the perimeter, which massively increase the space occupied by the fluid + air composite. Such an electrically inflatable foamy object could be applied to block slits that could be used as electrically actuated fluid valves for gas flow control.

5. Methods

In our studies, we used the liquid crystal 4-[(4-nitrophenoxy) carbonyl] phenyl-2,4-dimethoxybenzoate (RM734, purchased from Instec, USA), which is one of the prototype compounds for ferroelectric nematic materials. We dissolved 0.5 wt% of IR-1061 dye (Sigma-Aldrich) in RM734 to increase absorption of infrared light, although this feature is not exploited in the studies presented here. We confirmed that the effect of the small amount of dye (0.5 wt%) on the studied interfacial instabilities was negligible by obtaining the same results with undoped RM734 in different insulating layer thicknesses.

The FNLC drops were sandwiched between indium-tin-oxide (ITO) coated glass plates with an electrically insulating layer of SU8-3000 (Kayaku Microchem) on top of the ITO. The first step of sample preparation was cleaning the glass plates following a standard procedure: sonication in an alkaline detergent solution for 20 min, rinsing by deionized water (DI-H_2O) 5 times, sonication in DI-H_2O for two times 15 min, annealing in isopropanol steam at 90 °C, drying by clean air stream and plasma treatment in a plasma cleaner for 5 min. The preparation of the SU8 layers of different thickness was done in the following steps: spin coating of SU8-3050 dissolved in cyclopentanone at various concentrations at 500 rpm for 10 s and at 3000 rpm for 30 s, soft baking

Table 1
Thickness of the SU8 layer as a function of the solid content concentration of SU8 in cyclopentanone. The error was calculated as the largest deviation from the average measured on three samples.

SU8 wt% in cyclopentatone	Layer thickness (nm)
2 %	51 ± 6
5 %	260 ± 26
10 %	315 ± 32
18 %	750 ± 75
30 %	1500 ± 150
40 %	2966 ± 297
50 %	5788 ± 579

at 95 °C for 3 min, exposure by UV light for 1 min, post exposure baking at 95 °C for 3 min, developing in SU8 developer for 5 min, rinsing by isopropanol, and drying by cleaned air. The SU8 film thickness for each concentration (see Table 1) was measured by a Veeco Dektak 150 profilometer.

To create the liquid bridge, first a sessile droplet was placed on the substrate in the nematic phase at ~180 °C by a custom-made setup allowing micromanipulation and microscopic observation in side-view. After this, another SU8 coated plate was placed and glued on the top. Glass spacers mixed in the glue were applied to set the cell gap. The experiments were carried out by using a Nikon Eclipse Ti2-A inverted polarizing microscope equipped with a Instec HCS402 heating stage and an Instec mK1000 controller.

CRediT authorship contribution statement

Marcell Tibor Máthé: Writing – review & editing, Visualization, Software, Methodology, Investigation, Formal analysis, Data curation. **Hiroya Nishikawa:** Writing – review & editing, Validation, Methodology. **Fumito Araoka:** Writing – review & editing, Resources, Project administration, Funding acquisition. **Antal Jákli:** Writing – review & editing, Validation, Supervision, Resources, Project administration, Funding acquisition. **Péter Salamon:** Writing – review & editing, Writing – original draft, Supervision, Resources, Project administration, Methodology, Funding acquisition, Conceptualization.

Declaration of competing interest

The authors declare that they have no known competing financial interests or personal relationships that could have appeared to influence the work reported in this paper.

Data availability

Data will be made available on request.

Acknowledgement

This work was financially supported by the Hungarian National Research, Development, and Innovation Office under grants NKFIH FK142643, 2023-1.2.1-ERA_NET-2023-00008, the US National Science Foundation under grant DMR-2210083. The work was also supported by the János Bolyai Research Scholarship of the Hungarian Academy of Sciences (HAS) and a bilateral mobility project between HAS and the Japan Society for the Promotion of Science (JSPS). This work was partially supported by JSPS KAKENHI (JP22K14594; H.N., 23 K17341, JP21H01801; F.A.), RIKEN Special Postdoctoral Researchers (SPDR) fellowship (H.N.), FY2022 RIKEN Incentive Research Projects (H.N.), and JST CREST (JPMJCR17N1; F.A.) and JST SICORP EIG CONCERT-Japan (JPMJSC22C3; F.A.). The authors acknowledge fruitful discussions with Ágnes Buka.

Appendix A. Supplementary data

Supplementary data to this article can be found online at https://doi.org/10.1016/j.molliq.2024.126047.

References

[1] H. Nishikawa, K. Shiroshita, H. Higuchi, Y. Okumura, Y. Haseba, S. Yamamoto, K. Sago, H. Kikuchi, A Fluid Liquid-Crystal Material with Highly Polar Order, Adv. Mater. 29 (2017) 1702354, https://doi.org/10.1002/adma.201702354.
[2] R.J. Mandle, S.J. Cowling, J.W. Goodby, A nematic to nematic transformation exhibited by a rod-like liquid crystal, PCCP 19 (2017) 11429–11435, https://doi.org/10.1039/c7cp00456g.
[3] M. Born, Uber anisotrope Flussigkeiten: Versuch einer Theorie der flussigen Kristalle und des elektrischen Kerr-Effekts in Flussigkeiten, Sitzungsber. Preuss. Akad Wiss 30 (1916) 614–650.
[4] O.D. Lavrentovich, Ferroelectric nematic liquid crystal, a century in waiting, PNAS 117 (2020) 14629–14631, https://doi.org/10.1073/pnas.2008947117.
[5] R.J. Mandle, S.J. Cowling, J.W. Goodby, Rational Design of Rod-Like Liquid Crystals Exhibiting Two Nematic Phases, Chem. A Eur. J. 23 (2017) 14554–14562, https://doi.org/10.1002/chem.201702742.
[6] R.J. Mandle, N. Sebastián, J. Martinez-Perdiguero, A. Mertelj, On the molecular origins of the ferroelectric splay nematic phase, Nat. Commun. 12 (2021) 4962, https://doi.org/10.1038/s41467-021-25231-0.
[7] N. Sebastián, M. Čopič, A. Mertelj, Ferroelectric nematic liquid-crystalline phases, Phys. Rev. E 106 (2022) 21001, https://doi.org/10.1103/PhysRevE.106.021001.
[8] X. Chen, E. Korblova, D. Dong, X. Wei, R. Shao, L. Radzihovsky, M.A. Glaser, J. E. MacLennan, D. Bedrov, D.M. Walba, N.A. Clark, First-principles experimental demonstration of ferroelectricity in a thermotropic nematic liquid crystal: Polar domains and striking electro-optics, PNAS 117 (2020) 14021–14031, https://doi.org/10.1073/pnas.2002290117.
[9] M.T. Máthé, M.S.H. Himel, A. Adaka, J.T. Gleeson, S. Sprunt, P. Salamon, A. Jákli, Liquid Piezoelectric Materials: Linear Electromechanical Effect in Fluid Ferroelectric Nematic Liquid Crystals, Adv. Funct. Mater. (2024) 2314158, https://doi.org/10.1002/adfm.202314158.
[10] P. Medle Rupnik, L. Cmok, N. Sebastián, A. Mertelj, Viscous Mechano-Electric Response of Ferroelectric Nematic Liquid, Adv Funct Mater (2024) 2402554. https://doi.org/10.1002/adfm.202402554.
[11] P.G. de Gennes, J. Prost, The Physics of Liquid Crystals, Oxford University Press, Oxford, 1993.
[12] R. Saha, P. Nepal, C. Feng, M.S. Hossain, M. Fukuto, R. Li, J.T. Gleeson, S. Sprunt, R.J. Twieg, A. Jákli, Multiple ferroelectric nematic phases of a highly polar liquid crystal compound, Liq. Cryst. 49 (2022) 1784–1796, https://doi.org/10.1080/02678292.2022.2069297.
[13] T. Kumazawa, Y. Kumagai, H. Miura, M. Kitano, K. Kushida, Effect of external stress on polarization in ferroelectric thin films, Appl. Phys. Lett. 72 (1998) 608–610, https://doi.org/10.1063/1.120820.
[14] N. Sebastián, L. Cmok, R.J. Mandle, M.R. De La Fuente, I. Drevenšek Olenik, M. Čopič, A. Mertelj, Ferroelectric-Ferroelastic Phase Transition in a Nematic Liquid Crystal, Phys. Rev. Lett. 124 (2020) 037801, https://doi.org/10.1103/PhysRevLett.124.037801.
[15] A. Manabe, M. Bremer, M. Kraska, Ferroelectric nematic phase at and below room temperature, Liq. Cryst. 48 (2021) 1079–1086, https://doi.org/10.1080/02678292.2021.1921867.
[16] X. Zhao, J. Zhou, J. Li, J. Kougo, Z. Wan, M. Huang, S. Aya, Spontaneous helielectric nematic liquid crystals: Electric analog to helimagnets, Proceedings of the National Academy of Sciences 118 (2021) e2111101118. https://doi.org/10.1073/pnas.2111101118.
[17] A. Erkoreka, J. Martinez-Perdiguero, R.J. Mandle, A. Mertelj, N. Sebastián, Dielectric spectroscopy of a ferroelectric nematic liquid crystal and the effect of the sample thickness, J. Mol. Liq. 387 (2023) 122566, https://doi.org/10.1016/J.MOLLIQ.2023.122566.
[18] A. Erkoreka, A. Mertelj, M. Huang, S. Aya, N. Sebastián, J. Martinez-Perdiguero, Collective and non-collective molecular dynamics in a ferroelectric nematic liquid crystal studied by broadband dielectric spectroscopy, J. Chem. Phys. 159 (2023) 184502, https://doi.org/10.1063/5.0173813.
[19] S. Brown, E. Cruickshank, J.M.D. Storey, C.T. Imrie, D. Pociecha, M. Majewska, A. Makal, E. Gorecka, Multiple Polar and Non-polar Nematic Phases, ChemPhysChem 22 (2021) 2506–2510, https://doi.org/10.1002/cphc.202100644.
[20] N. Yadav, Y.P. Panarin, J.K. Vij, W. Jiang, G.H. Mehl, Two mechanisms for the formation of the ferronematic phase studied by dielectric spectroscopy, J. Mol. Liq. 378 (2023) 121570, https://doi.org/10.1016/J.MOLLIQ.2023.121570.
[21] J. Li, H. Nishikawa, J. Kougo, J. Zhou, S. Dai, W. Tang, X. Zhao, Y. Hisai, M. Huang, S. Aya, Development of ferroelectric nematic fluids with giant-dielectricity and nonlinear optical properties, Sci. Adv. 7 (2021) 5047–5068, https://doi.org/10.1126/SCIADV.ABF5047/SUPPL_FILE/ABF5047_SM.PDF.
[22] A. Erkoreka, N. Sebastián, A. Mertelj, J. Martinez-Perdiguero, A molecular perspective on the emergence of long-range polar order from an isotropic fluid, J. Mol. Liq. (2024) 125188, https://doi.org/10.1016/j.molliq.2024.125188.
[23] H. Nishikawa, K. Sano, F. Araoka, Anisotropic fluid with phototunable dielectric permittivity, Nat. Commun. 13 (2022) 1142, https://doi.org/10.1038/s41467-022-28763-1.
[24] M.T. Máthé, K. Perera, Á. Buka, P. Salamon, A. Jákli, Fluid Ferroelectric Filaments, Adv. Sci. 11 (2024) 2305950, https://doi.org/10.1002/ADVS.202305950.

[25] A. Jarosik, H. Nádasi, M. Schwidder, A. Manabe, M. Bremer, M. Klasen-Memmer, A. Eremin, Fluid fibers in true 3D ferroelectric liquids, Proceedings of the National Academy of Sciences 121 (2024) e2313629121. https://doi.org/10.1073/pnas.2313629121.
[26] F. Caimi, G. Nava, S. Fuschetto, L. Lucchetti, P. Paiè, R. Osellame, X. Chen, N. A. Clark, M.A. Glaser, T. Bellini, Fluid superscreening and polarization following in confined ferroelectric nematics, Nat. Phys. 19 (2023) 1658–1666, https://doi.org/10.1038/s41567-023-02150-z.
[27] A.M.J. Edwards, C.V. Brown, M.I. Newton, G. McHale, Dielectrowetting: The past, present and future, Curr Opin Colloid, Interface Sci. 36 (2018) 28–36, https://doi.org/10.1016/j.cocis.2017.11.005.
[28] G. McHale, C.V. Brown, N. Sampara, Voltage-induced spreading and superspreading of liquids, Nat. Commun. 4 (2013) 1605–1607, https://doi.org/10.1038/ncomms2619.
[29] G. McHale, C.V. Brown, M.I. Newton, G.G. Wells, N. Sampara, Dielectrowetting driven spreading of droplets, Phys. Rev. Lett. 107 (2011) 186101, https://doi.org/10.1103/PhysRevLett.107.186101.
[30] M.D. Cowley, R.E. Rosensweig, The interfacial stability of a ferromagnetic fluid, J. Fluid Mech. 30 (1967) 671–688, https://doi.org/10.1017/S0022112067001697.
[31] E. Ronald, Rosensweig, Cambridge University Press, Cambridge, Ferrohydrodynamics, 1985.
[32] M.T. Máthé, B. Farkas, L. Péter, Á. Buka, A. Jákli, P. Salamon, Electric field-induced interfacial instability in a ferroelectric nematic liquid crystal, Sci. Rep. 13 (2023) 6981, https://doi.org/10.1038/s41598-023-34067-1.
[33] R. Barboza, S. Marni, F. Ciciulla, F.A. Mir, G. Nava, F. Caimi, A. Zaltron, N.A. Clark, T. Bellini, L. Lucchetti, Explosive electrostatic instability of ferroelectric liquid droplets on ferroelectric solid surfaces, Proceedings of the National Academy of Sciences 119 (2022) e2207858119. https://doi.org/10.1073/pnas.2207858119.
[34] L. Cmok, V. Coda, N. Sebastian, A. Mertelj, M. Zgonik, S. Aya, M. Huang, G. Montemezzani, I. Drevensek-Olenik, Running streams of a ferroelectric nematic liquid crystal on a lithium niobate surface, Liq. Cryst. 50 (2023) 1478–1485, https://doi.org/10.1080/02678292.2022.2161018.
[35] R. Barboza, S. Bahwi, S. Marni, L. Lucchetti, On the Behavior of Ferroelectric Liquid Droplets in the Vicinity of a Ferroelectric Solid, Crystals 13 (2023) 750, https://doi.org/10.3390/CRYST13050750/S1.
[36] S. Marni, R. Barboza, A.S. Oluwajoba, R. Zamboni, L. Lucchetti, Polarization Coupling between Ferroelectric Liquids and Ferroelectric Solids: Effects of the Fringing Field Profile, Crystals 14 (2024) 425, https://doi.org/10.3390/cryst14050425.
[37] S. Marni, F. Caimi, R. Barboza, N. Clark, T. Bellini, L. Lucchetti, Fluid jets and polar domains, on the relationship between electromechanical instability and topology in ferroelectric nematic liquid crystal droplets, Soft Matter 20 (2024) 4878–4885, https://doi.org/10.1039/D4SM00317A.
[38] S. Marni, R. Barboza, A. Zaltron, L. Lucchetti, Optical control of mass ejection from ferroelectric liquid droplets: A possible tool for the actuation of complex fluids, J. Mol. Liq. 384 (2023) 122287, https://doi.org/10.1016/j.molliq.2023.122287.
[39] A. Sterle, L. Cmok, N. Sebastián, A. Mertelj, Y. Kong, X. Zhang, Drevenšek-Olenik, Light-induced dynamics of liquid-crystalline droplets on the surface of iron-doped lithium niobate crystals, Opt Mater, Express 13 (2023) 282–294, https://doi.org/10.1364/OME.477717.
[40] S. Marni, G. Nava, R. Barboza, T.G. Bellini, L. Lucchetti, Walking Ferroelectric Liquid Droplets with Light, Adv. Mater. 35 (2023) 2212067, https://doi.org/10.1002/adma.202212067.
[41] R.E. Rosensweig, M. Zahn, R. Shumovich, Labyrinthine instability in magnetic and dielectric fluids, J. Magn. Magn. Mater. 39 (1983) 127–132, https://doi.org/10.1016/0304-8853(83)90416-X.
[42] M.-H. Meurisse, M. Querry, Squeeze Effects in a Flat Liquid Bridge Between Parallel Solid Surfaces, J. Tribol. 128 (2006) 575–584, https://doi.org/10.1115/1.2197525.
[43] M.T. Máthé, H. Nishikawa, F. Araoka, A. Jákli, P. Salamon, Electrically activated ferroelectric nematic microrobots, Nat. Commun. 15 (2024) 6928, https://doi.org/10.1038/s41467-024-50226-y.
[44] N.A. Clark, X. Chen, J.E. MacLennan, M.A. Glaser, Dielectric spectroscopy of ferroelectric nematic liquid crystals: Measuring the capacitance of insulating interfacial layers, Phys Rev Res 6 (2024) 013195, https://doi.org/10.1103/PhysRevResearch.6.013195.
[45] A. Adaka, M. Rajabi, N. Haputhantrige, S. Sprunt, O.D. Lavrentovich, A. Jakli, Dielectric properties of a ferroelectric nematic material: quantitative test of the polarization-capacitance Goldstone mode, Phys. Rev. Lett. 133 (2024) 038101, https://doi.org/10.1103/PhysRevLett.133.038101.
[46] V. Matko, E. Gorecka, D. Pociecha, J. Matraszek, N. Vaupotič, Do ferroelectric nematic liquid crystals really have a huge dielectric permittivity? ArXiv (2024) 2401.16084, https://doi.org/10.48550/arXiv.2401.16084.
[47] M.T. Máthé, Á. Buka, A. Jákli, P. Salamon, Ferroelectric nematic liquid crystal thermomotor, Phys. Rev. E 105 (2022) L052701, https://doi.org/10.1103/physreve.105.l052701.
[48] B. Basnet, M. Rajabi, H. Wang, P. Kumari, K. Thapa, S. Paul, M.O. Lavrentovich, O. D. Lavrentovich, Soliton walls paired by polar surface interactions in a ferroelectric nematic liquid crystal, Nat. Commun. 13 (2022) 3932, https://doi.org/10.1038/s41467-022-31593-w.
[49] J. Yang, Y. Zou, W. Tang, J. Li, M. Huang, S. Aya, Spontaneous electric-polarization topology in confined ferroelectric nematics, Nat. Commun. 13 (2022) 7806, https://doi.org/10.1038/s41467-022-35443-7.
[50] E. Zavvou, M. Klasen-Memmer, A. Manabe, M. Bremer, A. Eremin, Polarisation-driven magneto-optical and nonlinear-optical behaviour of a room-temperature ferroelectric nematic phase, Soft Matter 18 (2022) 8804–8812, https://doi.org/10.1039/D2SM01298G.
[51] Y. Zou, J. Yang, X. Zhang, M. Huang, S. Aya, Topology of ferroelectric nematic droplets: the case driven by flexoelectricity or depolarization field, Soft Matter 20 (2024) 3392–3400, https://doi.org/10.1039/D3SM01042B.
[52] D.P. Jackson, B. Gantner, Energetics of interacting magnetized domains, Phys. Rev. E 64 (2001) 056230, https://doi.org/10.1103/PhysRevE.64.056230.
[53] D.P. Jackson, J.A. Miranda, Controlling fingering instabilities in rotating ferrofluids, Phys. Rev. E 67 (2003) 017301, https://doi.org/10.1103/PhysRevE.67.017301.
[54] D.P. Jackson, Orientational preference and predictability in a symmetric arrangement of magnetic drops, Phys. Rev. E 68 (2003) 035301, https://doi.org/10.1103/PhysRevE.68.035301.
[55] J.A. Miranda, R.M. Oliveira, D.P. Jackson, Adhesion phenomena in ferrofluids, Phys. Rev. E 70 (2004) 036311, https://doi.org/10.1103/PhysRevE.70.036311.
[56] D.P. Jackson, Theory, experiment, and simulations of a symmetric arrangement of quasi-two-dimensional magnetic fluid drops, J. Magn. Magn. Mater. 289 (2005) 188–191, https://doi.org/10.1016/j.jmmm.2004.11.055.
[57] N.J. Hillier, D.P. Jackson, Width of a ferrofluid finger: Hysteresis and a double energy minimum, Phys. Rev. E 75 (2007) 036314, https://doi.org/10.1103/PHYSREVE.75.036314/FIGURES/10/MEDIUM.
[58] D.P. Jackson, J.A. Miranda, Confined ferrofluid droplet in crossed magnetic fields, The, European Physical Journal E 23 (2007) 389–396, https://doi.org/10.1140/epje/i2007-10199-x.
[59] D.P. Jackson, Hysteresis and multiple stable configurations in a magnetic fluid system, J. Phys. Condens. Matter 20 (2008) 204140, https://doi.org/10.1088/0953-8984/20/20/204140.
[60] M. Zahn, R. Shumovich, Labyrinthine Instability in Dielectric Fluids, IEEE Trans. Ind. Appl. IA-21 (1985) 53–61, https://doi.org/10.1109/TIA.1985.349643.
[61] A.W. Adamson, A.G. Gast, Physical Chemistry of Surfaces, 6th ed., John Wiley & Sons Inc, New York, 1997.